scientific reports

Check for updates

OPEN

Ca^{+2} and Nε-lysine acetylation regulate the CALR-ATG9A interaction in the lumen of the endoplasmic reticulum

Megan M. Braun[1,2,3], Brendan K. Sheehan[1,2,7], Samantha L. Shapiro[1,2], Yun Ding[1,8], C. Dustin Rubinstein[4], Brent P. Lehman[4] & Luigi Puglielli[1,2,5,6]✉

The acetylation of autophagy protein 9 A (ATG9A) in the lumen of the endoplasmic reticulum (ER) by ATase1 and ATase2 regulates the induction of reticulophagy. Analysis of the ER-specific ATG9A *interactome* identified calreticulin (CALR), an ER luminal Ca^{+2}-binding chaperone, as key for ATG9A activity. Specifically, if acetylated, ATG9A is sequestered by CALR and prevented from engaging FAM134B and SEC62. Under this condition, ATG9A is unable to activate the autophagy core machinery. In contrast, when non-acetylated, ATG9A is released by CALR and able to engage FAM134B and SEC62. In this study, we report that Ca^{+2} dynamics across the ER membrane regulate the ATG9A-CALR interaction as well as the ability of ATG9A to trigger reticulophagy. We show that the Ca^{+2}-binding sites situated on the C-domain of CALR are essential for the ATG9A-CALR interaction. Finally, we show that K359 and K363 on ATG9A can influence the ATG9A-CALR interaction. Collectively, our results disclose a previously unidentified aspect of the complex mechanisms that regulate ATG9A activity. They also offer a possible area of intersection between Ca^{+2} metabolism, acetyl-CoA metabolism, and ER proteostasis.

Keywords Proteostasis, Reticulophagy, Lysine acetylation, Calcium, Calreticulin, ATG9A

The endoplasmic reticulum (ER) acetylation machinery has emerged as a fundamental branch of the general nutrient-signaling pathway, which enables rapid modulation and reprogramming of different intracellular activities upon fluctuation of metabolites/nutrients[1–3]. Specifically, Nε-lysine acetylation in the lumen of the ER maintains protein homeostasis (proteostasis), thus connecting the intracellular flux of citrate/acetyl-CoA to the efficiency of the secretory pathway[1]. Essential mediators of the above flux are SLC13A5, SLC25A1, ACLY, AT-1/SLC33A1, ATase1/NAT8B, and ATase2/NAT8. SLC13A5 and SLC25A1 import citrate to the cytosol, respectively from the extracellular *milieu* and the mitochondria; ACLY converts cytosolic citrate to acetyl-CoA, while AT-1 ensures translocation of cytosolic acetyl-CoA into the ER lumen. Finally, the ATases use acetyl-CoA to acetylate ER-cargo and -resident proteins (reviewed in[1]).

An essential component of the proteostatic functions of the ER acetylation machinery is the induction of ER-specific autophagy (often referred to as reticulophagy or ER-phagy) to ensure disposal of toxic protein aggregates that form in the ER (reviewed in[1]). This is achieved by regulating the acetylation status of autophagy protein 9 A (ATG9A) within the ER lumen[4]. Mouse models of ER hyperacetylation display increased acetylation of ATG9A and a block of reticulophagy, while mouse models of hypoacetylation display the opposite[5–8]. Finally, biochemical inhibition of the ATases in mice with ER hyperacetylation rescues the hyperacetylation status of ATG9A and reactivates reticulophagy[6–10]. In humans, defective ER acetylation - as caused by loss-of-function mutations or gene duplication events - is associated with different diseases spanning from developmental

[1]Department of Medicine, School of Medicine and Public Health, University of Wisconsin-Madison, Madison, WI 53705, USA. [2]Waisman Center, University of Wisconsin-Madison, 1500 Highland Ave, Madison, WI 53705, USA. [3]Neuroscience Training Program, University of Wisconsin-Madison, Madison, WI 53705, USA. [4]Biotechnology Center, University of Wisconsin-Madison, Madison, WI 53706, USA. [5]Geriatric Research Education Clinical Center, Veterans Affairs Medical Center, Madison, WI 53705, USA. [6]Department of Neuroscience, School of Medicine and Public Health, University of Wisconsin-Madison, Madison, WI 53705, USA. [7]Present address: Case Western Reserve University, Cleveland, OH 44106, USA. [8]Present address: Lilly Oncology, San Diego, CA 92121, USA. ✉email: lp1@medicine.wisc.edu

delay and premature death to peripheral neuropathy, autism spectrum disorder with intellectual disability and dysmorphism (reviewed in[1]). These disease phenotypes are efficiently mimicked in the mouse[5,6,8,11–13].

We recently used unbiased mass spectrometry to resolve the ATG9A *interactome* on the ER surface[14]. While doing this, we discovered that the acetylation status of the ER regulates the ATG9A-CALR interaction within the ER lumen, and that this interaction corresponds to the ability of ATG9A to engage the cytosolic C-end of FAM134B and SEC62[14]. CALR is an ER luminal protein and has both high-affinity and low-affinity Ca^{+2}-binding sites; FAM134B and SEC62 are ER membrane proteins with Ca^{+2}-binding helix-loop-helix EF hands on their cytosolic C-end. The fact that Ca^{+2}-binding elements are positioned on fundamental ATG9A-binding partners on the opposite sides of the ER membrane suggests that variations in Ca^{+2} dynamics across the ER membrane might regulate the ability of ATG9A to trigger reticulophagy. In this study, we report that Ca^{+2} dynamics across the ER membrane indeed regulate the ATG9A-CALR interaction as well as the ability of ATG9A to trigger reticulophagy. We show that the Ca^{+2}-binding sites situated on the C-domain of CALR are essential for the ATG9A-CALR interaction. Finally, we reinforce the concept that K359 and K363, the two ATG9A lysine residues that have been shown to be acetylated, can influence the CALR-ATG9A interaction. Collectively, our results reveal a novel aspect of the complex mechanisms that regulate ATG9A activity and offer a possible area of intersection between Ca^{+2} metabolism, acetyl-CoA metabolism, and ER proteostasis.

Results

Ca^{+2} dynamics in the ER regulate the induction of reticulophagy

To initially test regulatory functions of Ca^{+2} dynamics across the ER membrane, we used HEK293 cells with stable expression of the ER autophagy tandem reporter (EATR) probe, which includes a tandem mCherry-eGFP reporter fused to RAMP4 (Fig. 1A). Since RAMP4 is an integral ER-membrane resident protein, EATR specifically detects induction of reticulophagy[14,15]. The cells (referred to as HEK293-EATR thereafter) were treated with several already validated Ca^{+2} modifying drugs to visualize activation or inhibition of reticulophagy by flow cytometry (Fig. 1B-E). Induction of reticulophagy was consistently observed following treatment with Thapsigargin (Tg, 1μM) and Ionomycin (Io, 2–4μM), while a block in induction was observed with Trifluoperazine (TFP, 3μM). Tg is a non-competitive inhibitor of the sarcoplasmic/endoplasmic reticulum Ca^{+2} ATPase (SERCA), an ER-based channel that ensures Ca^{+2} influx into the ER; Io is an ionophore and is used to increase cytosolic levels of Ca^{+2}; TFP is an antipsychotic drug that inhibits calmodulin and destabilizes cytosolic levels of $Ca^{[+2}$ [16,16]. Carbachol is an acetylcholine analog while CDN1163 is an allosteric SERCA activator with metabolic activity. Therefore, when taken together, the results suggest that a shift in Ca^{+2} dynamics across the ER membrane can influence the induction of reticulophagy. Specifically, depletion of ER Ca^{+2} stores in favor of the cytosol (i.e., with Tg and Io) stimulates reticulophagy while the opposite (i.e., with TFP) prevents reticulophagy (Fig. 1F). To confirm these outcomes, we transiently expressed HEK293-EATR cells with either SERCA2B - to pump Ca^{+2} into the ER - or inositol 1,4,5-triphosphate receptor type 3 (ITPR3) - to stimulate Ca^{+2} release from the ER (Fig. 1F). Expression of SERCA2B reduced while expression of ITPR3 increased the induction of reticulophagy (Fig. 1G-J), thus confirming the outcomes elicited by the Ca^{+2} modifying drugs (Fig. 1B-E).

The ATG9A-CALR interaction is modulated by the Ca^{+2} binding capacity of CALR

We recently identified CALR, an ER luminal Ca^{+2}-binding chaperone, as a novel ATG9A-interacting protein that influences the ability of ATG9A to recruit LC3β and activate reticulophagy[14]. CALR has high-affinity/low-capacity and low-affinity/high-capacity Ca^{+2}-binding sites that can hold about half of the total Ca^{+2}-loading capacity of the ER (Fig. 2A). Importantly, the structure of CALR is heavily modulated by Ca^{+2}-binding[18]. To test whether the Ca^{+2}-binding capacity of CALR dictates its ability to interact with ATG9A, we co-expressed ATG9A with Ca^{+2}-binding mutant versions of CALR. Both the D328A substitution, which eliminates the high-affinity/low-capacity Ca^{+2}-binding site, and the deletion of the entire 338-408aa (Δ338–408) α-helix, which eliminates the low-affinity/high-capacity Ca^{+2}-binding region, reduced the ATG9A-CALR interaction (Fig. 2B-E). This effect was observed when we probed for either ATG9A or CALR. Furthermore, the immunoprecipitation of CALR only pulled down the ER-based immature form of ATG9A, confirming that the ATG9A-CALR interaction occurs within the ER lumen, as previously demonstrated[14]. Finally, the effect of D328A substitution and the Δ338–408 deletion displayed additive effect, supporting the conclusion that the Ca^{+2} capacity of CALR is fundamental for the ATG9A-CALR interaction (Fig. 2F-G).

Next, we incubated affinity-purified CALR with two different concentrations of Ca^{+2} (5 mM and 20 mM) to reflect different Ca^{+2} load-capacity states that are observed in the ER[18]. The folding status of CALR was then analyzed with circular dichroism, which measures the difference in the absorbances of left- and right-handed circularly polarized light. The presence of Ca^{+2} caused rapid and marked changes in both absorption and ellipticity of CALR, reflecting structural changes in the α helix/β strand conformation from the no-Ca^{+2} to high-Ca^{+2} status (Fig. 2H). The spectra obtained is very similar to a previous one, which documented Ca^{+2}-mediated changes in the secondary structure of CALR and a differential contribution of the N-terminal β-sheets and the C-terminal α-helical segment where Ca^{+2} was able to force a disorder-to-structured transition[18].

To test the functional role of the Ca^{+2} binding capacity of CALR, we used CRISPR-Cas9 to introduce both the D328A substitution and the Δ338–408 deletion within the endogenous CALR of HEK293-EATR cells. The results show increased induction of reticulophagy in the mutant (referred to as $CALR^{CR}$) as compared to the wild type (WT cells, Fig. 2I). Importantly, this effect was observed with and without EBBS-induced starvation indicating that the Ca^{+2} binding capacity of CALR is required for CALR to control the induction of both basal and starvation-induced reticulophagy.

The results presented so far indicate that changes in Ca^{+2} dynamics across the ER membrane can regulate the induction of reticulophagy (see Fig. 1). They also indicate that the ATG9A-CALR interaction, which influences the ability of ATG9A to stimulate reticulophagy downstream of the ER acetylation machinery[14], is heavily

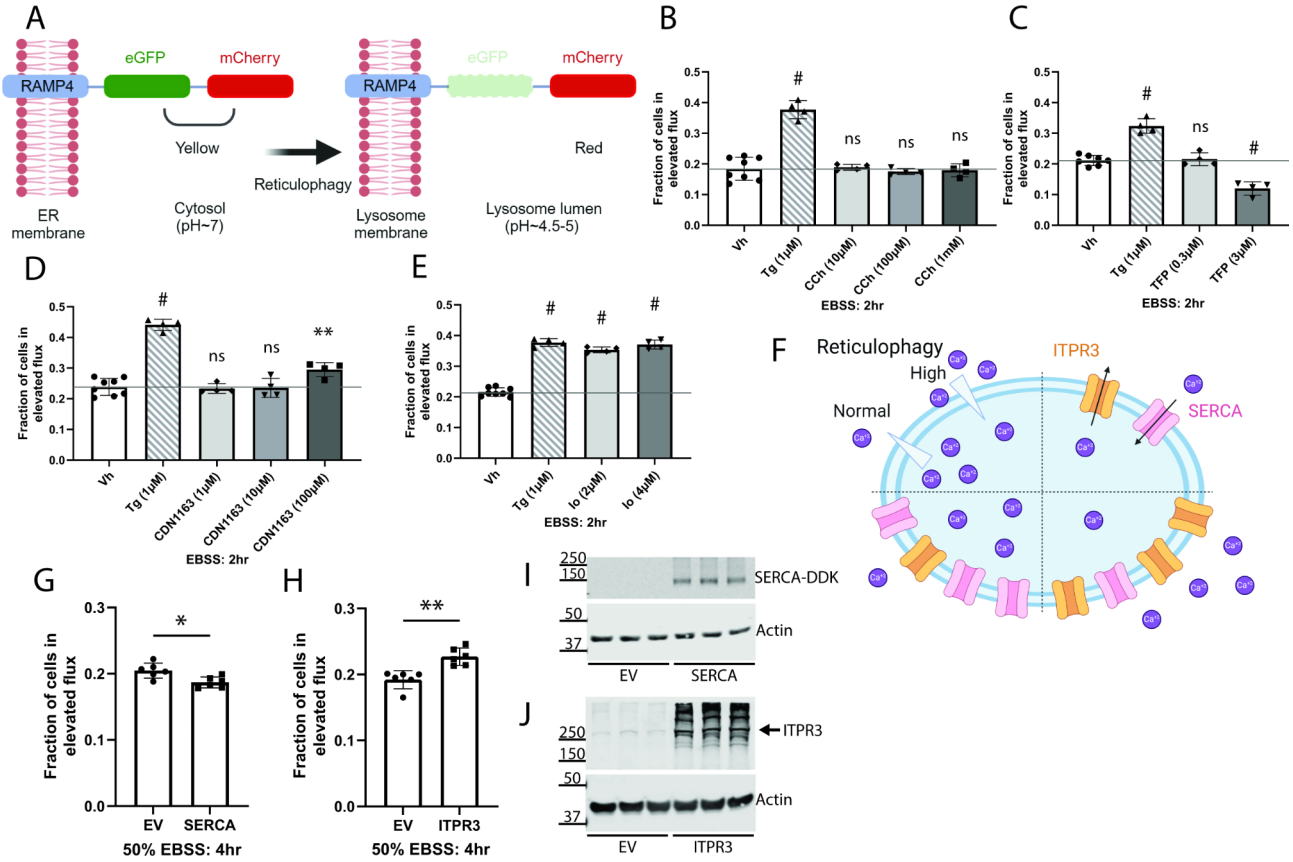

Fig. 1. Chemical and genetic modulators of ER luminal Ca^{+2} levels modulate reticulophagy induction. (**A**) Schematic demonstrating the EATR probe and assay mechanism (Image was generated using BioRender). (**B-E**) Flow cytometry analysis for elevated reticulophagy flux in HEK293-EATR cells treated with Ca^{+2}-modifying drugs: Thapsigargin (Tg), Carbachol (CCh), Trifluoperazine (TFP), CDN1163, and Ionomycin (Io). Vehicle (Vh, 0.1% DMSO) treated cells served as a control. (**F**) Schematic showing predicted impact of ITPR3 and SERCA overexpression on luminal Ca^{+2} levels and reticulophagy (Image was generated using BioRender). (**G-H**) Flow cytometry analysis for elevated reticulophagy flux in HEK293-EATR cells transiently overexpressing ER Ca^{+2} transporters SERCA and ITPR3. (**I-J**) Representative Western blots demonstrate overexpression of Ca^{+2} transporters in HEK293 EATR cells. Cells transfected with the empty vector (EV) served as the control. Data are represented as mean ± SD. $^{*}p < 0.05$, $^{**}p < 0.01$, $^{\#}p < 0.0001$ via ordinary one-way ANOVA with Dunnett's multiple comparison test (**B-E**) or Student's *t* test (**G-H**). Each point represents an independent biological sample.

regulated by the Ca^{+2}-binding capacity of CALR, most likely caused by Ca^{+2}-driven conformational changes (see Fig. 2). Finally, they support the argument that the Ca^{+2} binding capacity of CALR has reticulophagy-regulatory functions (see Fig. 2). In essence, we could envision a model where release of Ca^{+2} by the ER would reduce the CALR-Ca^{+2} binding, forcing a structured-to-unstructured transition of CALR with consequent dissociation of the ATG9A-CALR complex. This would release ATG9A and allow it to trigger the induction of reticulophagy.

K359 and K363 influence the CALR-ATG9A interaction

CALR is an ER luminal chaperone; therefore, the ATG9A-CALR interaction can only occur within the lumen of the ER. Consistently, immunoprecipitation of CALR exclusively pulled down the ER-based immature form of ATG9A (see Figs. 1 and 2). We previously reported that ATG9A is acetylated on two lysine residues, K359 and K363[4]. We also reported that the acetylated status of ATG9A in vivo correlated with the induction of reticulophagy. This was shown both in cellular and animal models[4,6–8,14]. Therefore, it is likely that K359 and K363 are required for the ATG9A-CALR interaction.

To test the above hypothesis, we removed both K359 (ΔK359) and K363 (ΔK363). The ΔK359/ΔK363 modification increased the ATG9A-CALR interaction (Fig. 3A-B). Importantly, the ΔK359/ΔK363 mutations yielded one ATG9A migrating as the immature, ER-based form of ATG9A, which would reflect the inability of ATG9A to leave the ER and reach the Golgi apparatus. Indeed, in contrast to $ATG9A_{WT}$, $ATG9A_{\Delta K359/\Delta K363}$ was found to be restricted to the ER on confocal microscopy (Fig. 3C-D).

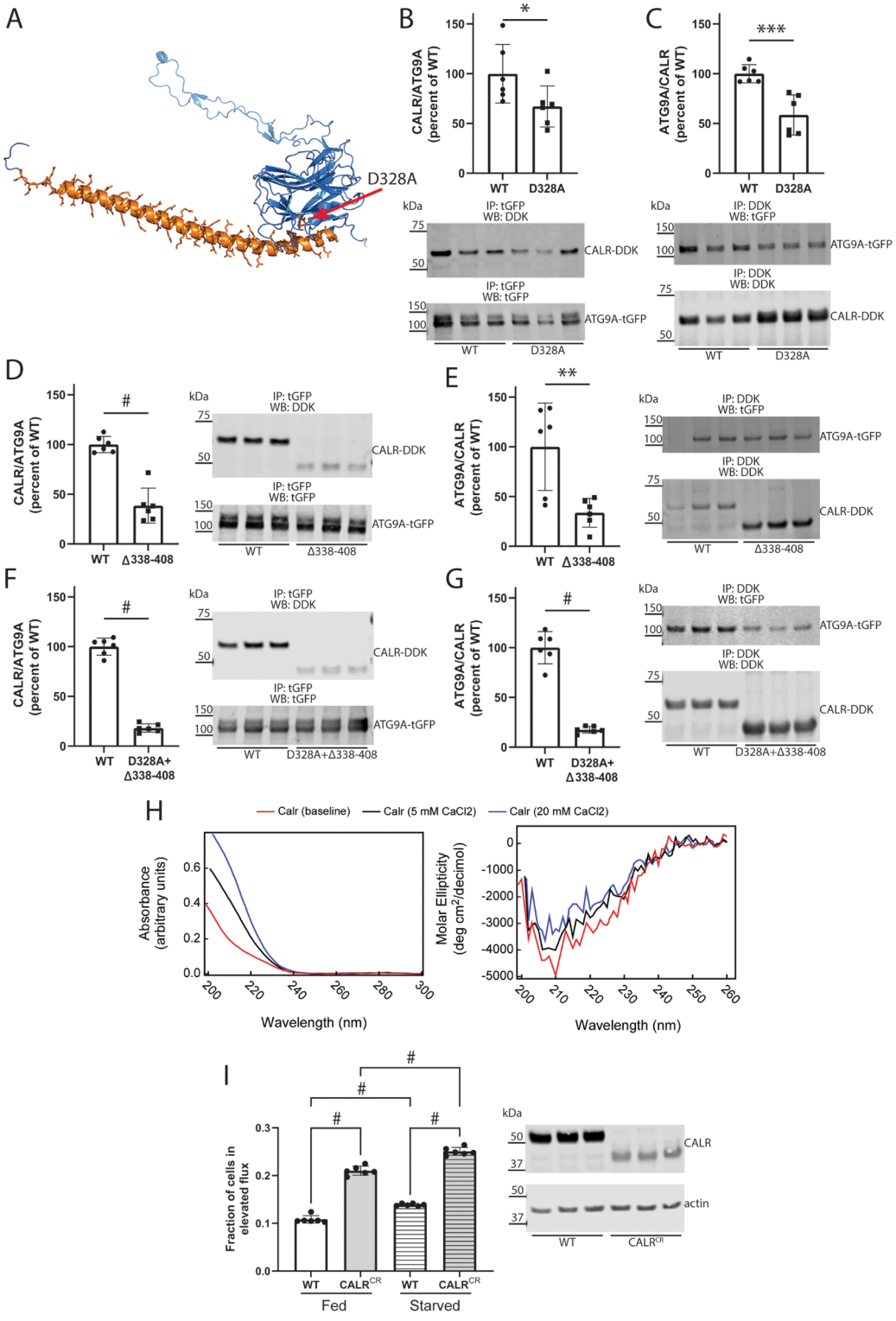

The influx of acetyl-CoA into the ER by AT-1 regulates the ER-exit of ATG9A

The results displayed so far indicate that, when bound to CALR, ATG9A is restricted to the ER and prevented from inducing reticulophagy. We have previously reported that the ATG9A-CALR complex is favored by ATG9A hyperacetylation in AT-1 sTg mice and inhibited by ATG9A hypoacetylation in AT-1$^{S113R/+}$ mice, which display reduced and increased induction of reticulophagy, respectively[14]. To test whether differential CALR-engagement states determine the ability of ATG9A to exit the ER under models of ER hyper- and hypo-acetylation and in the absence of mutations targeting either CALR or ATG9A, we determined the distribution profile of ATG9A in mouse embryonic fibroblasts (MEFs) derived from AT-1 hyper-and hypo-morphic mice. Consistent with the aforementioned model, we discovered that, under steady-state conditions, ATG9A preferentially co-localizes with SEC13 in AT-1 sTg MEFs (Fig. 4A-B). SEC13 is an ER protein involved with the biogenesis of ER exit sites (ERES)/COPII coats, and we previously reported that the ER-specific ATG9A interactome includes ERES/

◂**Fig. 2**. Ca^{+2}-binding sites on CALR are required to maintain normal binding with ATG9A. (**A**) Structural model of CALR (AF-P27797-F1) showing Ca^{+2} binding sites in orange. (**B**-**G**) Co-immunoprecipitation of ATG9A and CALR in HEK293 cells overexpressing tGFP tagged ATG9A and WT or mutant DDK tagged CALR. CALR mutations targeted the high-affinity/low-capacity Ca^{+2}-binding site (D328A; see arrow in *panel A*) and the low-affinity/high-capacity Ca^{+2}-binding α-helix (Δ338–408; shown in orange in *panel A*). Representative Western blots and accompanying quantification, normalized to the IP-ed protein, are shown. The upper band of the ATG9A blots corresponds to the mature, glycosylated form whereas the lower band corresponds to the immature, unglycosylated form that is found in the ER. Data are represented as mean ± SD. $^{*}p < 0.05$, $^{**}p < 0.01$, $^{***}p < 0.001$, $^{\#}p < 0.0001$ via Student's *t* test. (**H**) Absorbance and molar ellipticity of CALR incubated with 0 mM, 5 mM, or 20 mM $CaCl_2$ as measured with circular dichroism. (**I**) Flow cytometry analysis for elevated reticulophagy flux in CRISPR-modified HEK293 EATR cells (*left panel*). $CALR^{CR}$ cells have targeted mutations to both CALR Ca^{+2} binding sites and the WT cells are no-guide controls. Media was changed to fresh complete DMEM for the fed condition and to EBSS for the staved condition 2 h prior to flux analysis. Western blot (*right panel*) shows the migration profile of $CALR^{CR}$. Data are represented as mean ± SD. $^{*}p < 0.05$, $^{**}p < 0.01$, $^{***}p < 0.001$, $^{\#}p < 0.0001$ via Student's *t* test (**B**-**G**) or ordinary one-way ANOVA with Sidak's multiple comparison test (**I**). Each point represents an individual biological sample.

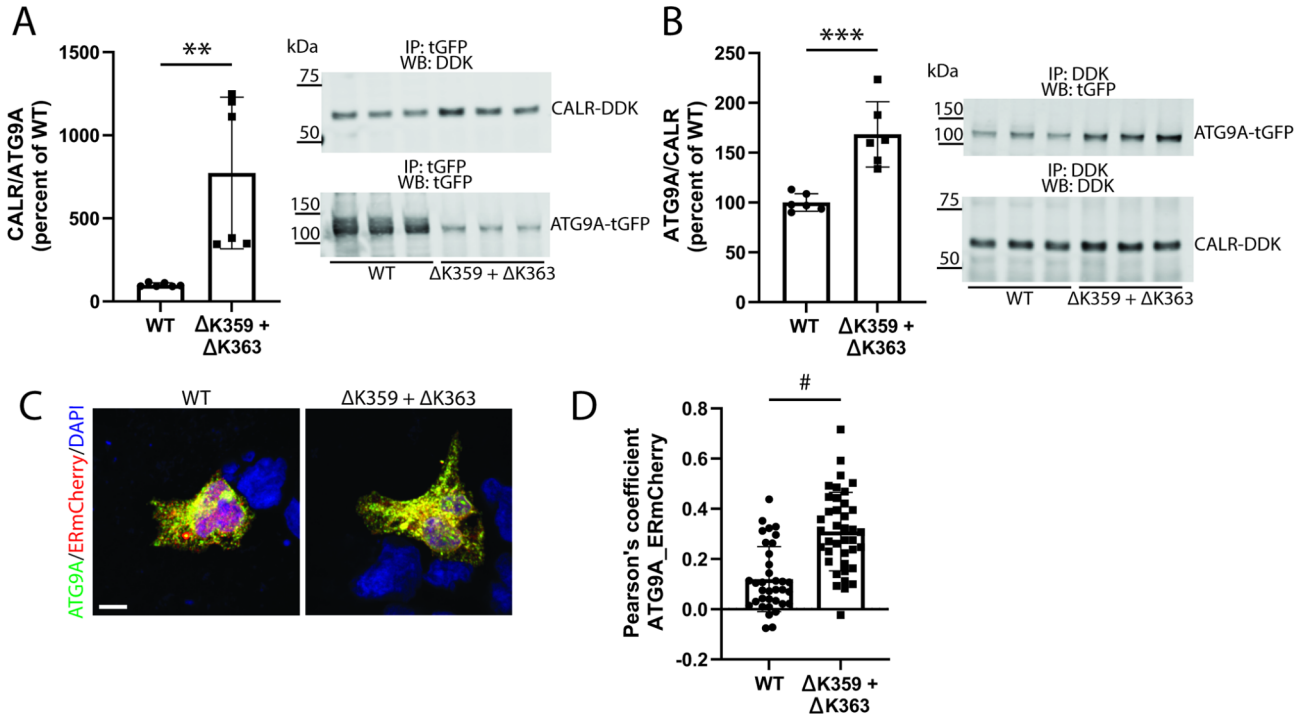

Fig. 3. ATG9A endoluminal acetylation mediates interaction with CALR and subcellular localization. (**A**-**B**) Co-immunoprecipitation of CALR and ATG9A in HEK293 cells overexpressing DDK tagged CALR and WT or mutant tGFP tagged ATG9A. Representative Western blots and accompanying quantification, normalized to the interaction between CALR and WT ATG9A, are shown. Each point represents an individual biological sample. (**C**-**D**) Representative images and accompanying Pearson's colocalization analysis for HEK293 cells transiently expressing ATG9A-tGFP and ERmCherry. Each point represents a cell (WT $n = 35$; ΔK359 + ΔK363 $n = 39$). Data are represented as mean ± SD. $^{*}p < 0.05$, $^{**}p < 0.01$, $^{***}p < 0.001$, $^{\#}p < 0.0001$ via Student's *t* test or ordinary one-way ANOVA with Sidak's multiple comparison test.

COP members[14]. The different behavior of ATG9A in MEFs with increased or reduced ER acetylation was further manifested under conditions of starvation-induced reticulophagy, where ATG9A demonstrated higher efficiency in exiting the ER in AT-$1^{S113R/+}$ MEFs (Fig. 4C-D).

Discussion

Under steady-state conditions, ATG9A is found in multiple cellular locations, including the ER, the Golgi apparatus, the plasma membrane, and the autophagosome[19–24]. Isolation of ATG9A from these different locations has yielded different proteins, suggesting that the ATG9A *interactome* closely reflects its cellular location[14,25–27]. The ability of ATG9A to transition across different cellular locations is likely to be dictated by different protein-protein interactions that are established in these different locations. By using unbiased mass spectrometry, we recently discovered that while on the ER membrane, ATG9A tightly associates with CALR, a Ca^{+2}-binding

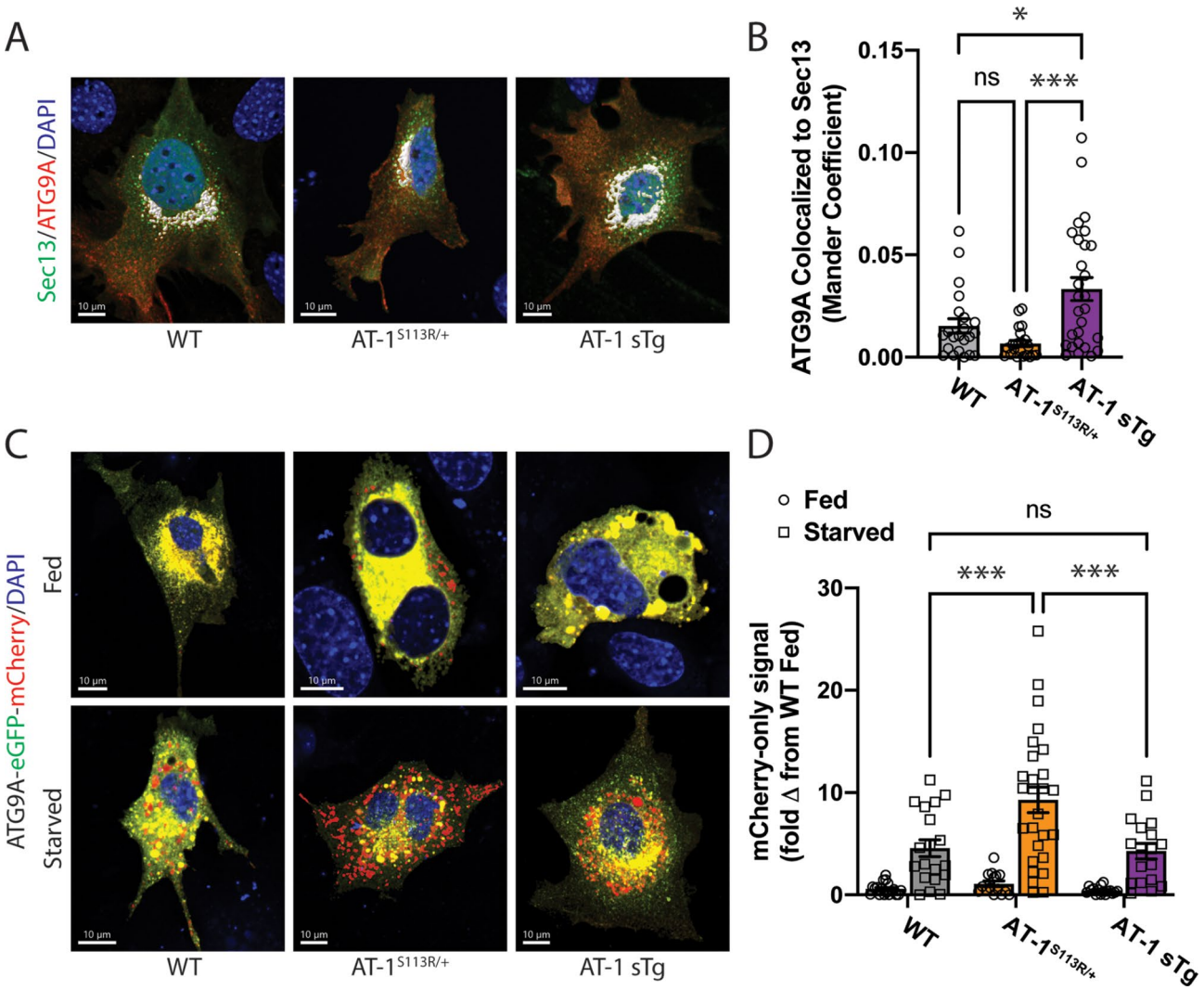

Fig. 4. Acetyl-CoA import by AT-1 modulates ATG9A ER exit. (**A**) Representative images of WT, AT-1$^{S113R/+}$, and AT-1 sTg derived MEFs transiently co-expressing SEC13-tGFP and ATG9A-mCherry. Colocalized volume are represented in white. (**B**) Mander's coefficient of ATG9A volume colocalized to SEC13 volume in MEFs (WT $n=22$; AT-1$^{S113R/+}$ $n=22$; AT-1 sTg $n=28$). (**C**) Representative live-cell images of WT, AT-1$^{S113R/+}$, and AT-1 sTg derived MEFs expressing ATG9A-eGFP-mCherry reporter probe in fed (DMEM) and starved (4 h, EBSS) conditions. Lysosomal pH quenches eGFP fluorescence. (**D**) IMARIS quantification of mCherry-only signal (not colocalized with eGFP) in MEFs (WT fed $n=18$, starved $n=19$; AT-1$^{S113R/+}$ fed $n=15$, starved $n=27$; AT-1 sTg fed $n=16$, starved $n=18$). Data are represented as mean ± SEM. $^{*}p<0.05$, $^{***}p<0.001$ via ordinary one-way ANOVA with Tukey's multiple comparisons test. Each point represents measurements from a single cell, with 3 biologically independent cell lines used for each genotype.

luminal chaperone[14]. Importantly, the ATG9A-CALR association was observed with endogenous proteins and closely matched to the acetylation status of the ER, as determined by the rate of acetyl-CoA transport into the ER lumen[14]. The ability of ATG9A to engage CALR within the lumen of the ER inversely correlated with its ability to engage FAM134B and SEC62 on the cytosolic side of the organelle[14]. CALR, FAM134B and SEC62 all have in common their ability to bind $Ca^{[+2}$[14,18]. Furthermore, the ER is the organelle with the highest concentration of Ca^{+2}, and changes in Ca^{+2} dynamics define different ER states[16,28]. Therefore, it is plausible to speculate that Ca^{+2} dynamics across the ER membrane might regulate the ability of ATG9A to transition out of the ER and trigger reticulophagy. This is illustrated in the present study.

Mechanistically, Ca^{+2} regulates both the ability of CALR to engage ATG9A (present study) and the ability of ATG9A to engage FAM134B and SEC62[14]. The ATG9A-CALR interaction occurs in the luminal side of the ER while the ATG9A-FAM134B and ATG9A-SEC62 interaction occurs on the cytosolic side of the organelle (present study and[14]). The fact that these two Ca^{+2}-driven events occur on the opposite sides of the ER membrane reinforces the argument that Ca^{+2} dynamics across the ER membrane regulate ATG9A functions.

All ATG9A proteins, from yeast to mammals, display a high degree of sequence conservation and they are all predicted to contain six transmembrane (TM) helices with three loops facing the luminal side. However,

the cryo-EM structure of ATG9A indicates that ATG9A can assemble as a trimer with a central open pore that is key to its autophagy-related activity[29–32]. The acetylated loop appears to be centrally located within the pore[29–32]. We could envision a dynamic model where engagement of CALR with the acetylated loop determines the multimeric assembly of ATG9A. Specifically, when bound to CALR, ATG9A would be unable to assemble into the trimeric structure, while when free of CALR, ATG9A would be able to exit the ER and assemble into the trimeric structure. The ATG9A-CALR interaction would be stabilized by structural features that depend on Ca^{+2}, through CALR, and Nε-lysine acetylation, through ATG9A. Although intriguing and supported by different mouse models, several mechanistic features of the above model remain elusive. This limitation is mostly caused by the fact that we still do not know how lysine acetylation can affect the domain structure of the modified protein to elicit its biological outcomes.

Within the cell, Ca^{+2} is stored in different organelles and compartments, and can be released/moved in response to different signals to trigger different biological messages. Ca^{+2} movements are closely related to the induction of autophagy from different compartments. The present manuscript offers a possible area of intersection between Ca^{+2} metabolism, acetyl-CoA metabolism, and ER proteostasis.

Methods

Cell culture

HEK293 (human embryonic kidney; RRIK: CVCL_0045) cells were grown in Dulbecco's modified Eagle's medium (Corning, 10-013-CV) supplemented with 10% Fetal Bovine Serum (Corning, 35-011-CV) and 1% penicillin/streptomycin (Gibco, 10378016), hereafter referred to as complete DMEM, in an incubator maintained at 37 °C with a humidified atmosphere and 5% CO_2. Cells were obtained and authenticated by the American Type Culture collection and are not listed as commonly misidentified cell line by the International Cell Line Authentication Committee (ICLAC, Version 9). Unless otherwise specified, cells were harvested as follows: trypsin-EDTA (Thermo Fisher Scientific, 25200072) was used to detach cells, DMEM was used to quench the reaction, cells were pelleted by centrifugation at 1,000 RPM for 5 min and washed twice with PBS.

Mouse embryonic fibroblast isolation

Isolation of mouse embryonic fibroblasts, MEFs, was previously described[5,33]. Briefly, embryos from timed pregnant females were collected at embryonic day 13.5 (E13.5). Embryos (without heads or visceral organs) were minced and incubated with trypsin-EDTA at 37 °C and 5% CO_2 for 30–45 min. Trypsin was quenched by adding complete DMEM and tissue was further disrupted by gentle pipetting. Cells suspended in media were passed through at 70 µm filter to create a single cell suspension. Cells were left in the incubator undisrupted for 24 h to attach and proliferate before preparing for long-term storage in freezing medium.

AT-1 sTg and AT-$1^{S113R/+}$ mice were described before[5,6] and donated to MMRRC (MMRRC:0681290-MU and MMRRC:068120-MU). Euthanasia of pregnant females was performed by CO_2 inhalation while the euthanasia of embryos was performed by decapitation. Both methods are approved by the American Veterinary Medical Association. All animal experiments were done according to the National Institutes of Health Guide for the Care and Use of Laboratory Animals and approved by the UW-Madison committee for animal care (protocol #M005120). All methods are in accordance with ARRIVE guidelines.

EATR assay

HEK293 cells stably over expressing SspI digested TetOn-mCherry-eGFP-RAMP4 vector (here after referred to as HEK293 EATR) were previously generated[14] and were maintained in complete DMEM with 400 µg/mL G418 (InvivoGen, ant-gn-1). Cells were plated on 12-well plates three days prior to flow cytometry analysis. One day prior to analysis, media was changed and, for the over expression experiments, cells were transfected. To stimulate autophagy, cells were incubated with 50% complete DMEM and 50% EBSS (Cytivia, SH30029.02) for 4 h. Alternatively, for the calcium-modulating experiments, cells were incubated with 100% EBSS for 2 h, and immediately after media change, cells were treated with a 10x solution containing calcium modulating agent (Tg, Sigma, T9033; CCH, Sigma, 212385; TFP, Sigma, T8516; CDN1163, Sigma, SML1682; Io, Sigma, 407950) or DMSO (vehicle). Post starvation, cells were trypsinized, centrifuged, and resuspended in DPBS (Lonza, 17–515 F) containing 2% FBS, 10 mM EDTA, and 1 µg/mL DAPI on ice. Flow cytometry was performed on Attune NxT flow cytometers (Thermo Fisher Scientific) configured with 405, 488, 561, and 637 nm lasers. The experimental population was defined with single, live, and mCherry-expressing gates. In-house python scripts were used to define "elevated flux" as followed: events one standard deviation above the least-squares regression line of eGFP vs. mCherry plot of non-transfected/vehicle cells incubated in 100% complete DMEM.

Cell transfection

HEK293 cells were transiently transfected with Lipofectamine 3000 (Invitrogen, 2773051) and MEFs were transiently transfected with Lipofectamine STEM (Invitrogen, 01108889), according to manufacturer's recommendations. Commercial plasmids used: human pCMV6-SERCA-DDK (Origene, RC207626), human pCMV6-ITPR3-DDK (Origene, RC222737), human pCMV6-ATG9A-DDK (Origene, RC222513), human pCMV6-ATG9A-tGFP (Origene, RG222568), human pCMV6-CALR-DDK (Origene, RC203222), ER signal sequence-ERmCherry-KDEL (gift from Michael Davidson, Addgene Plasmid, 55041), human pCMV6-SEC13-DDK (Origene, RC222811), TetOn-mCherry-eGFP-RAMP4 vector (hereafter referred to as EATR, gift from Jacob Corn; Addgene plasmid 109014), and pCMV6-Entry (OriGene, PS100001). Co-transfected cells received equal copy numbers of each plasmid.

Plasmid construction and site-directed mutagenesis

To generate the SEC13-tGFP plasmid, SEC13-DDK and ATG9A-tGFP were restriction enzyme digested with Asis and MluI. The SEC13 insert and the pCMV6-tGFP vector were gel purified and ligated with T4 ligase. To generate the ATG9A-EATR plasmid, the mCherry-eGFP fluorophores were PCR amplified from the EATR plasmid, and the 1.5 kb band was gel purified. The 1.5 kb band and pCMV6-ATG9A-DDK were restriction digested with NotI and FseI and ligated with T4 ligase. To generate ATG9A-mCherry, site directed mutagenesis was performed using QuickChange Lightning Multi Site-Directed Mutagenesis kit (Aligent Technologies, 210515 and 210513) per manufacturer's instructions to remove the endogenous MluI site and add a MluI site directly after mCherry in the ATG9A-EATR plasmid. The mutated ATG9A-EATR plasmid and ATG9A-pCMV6 were restriction enzyme digested by AsisI and MluI. The ATG9A-mCherry insert and the pCMV6 vector were gel purified and ligated with T4 ligase. The remaining constructs were generated by site-directed mutagenesis using QuickChange Lightning Site-Directed Mutagenesis kit (Aligent Technologies, 210518 and 210519) or Q5 Site-Directed Mutagenesis kit (NEB, E0554S) as indicated in Supplementary Table 1. Constructs were propagated from a single colony and plasmid DNA was extracted with QIAprep Spin Miniprep Kit or QIAGEN Plasmid Maxi Kit (Qiagen, 27106 and 12165). All primers used for plasmid construction are listed in Supplementary Table 1. Constructs were confirmed by DNA sequencing.

Co-immunoprecipitation and Western blotting

Protein extracts were prepared in GTIP buffer (10 mM Tris, pH 7.6; 2 mM EDTA, 0.15 M NaCl) supplemented with 1% Trition X-100 (Roche Applied Sciences, 11332481001), 0.25% Nonidet P-40 (Sigma, N-6507), and cOmplete, mini, EDTA-free protease inhibitor cocktail (Roche Applied Sciences, 11836170001). For immunoprecipitation, 0.15 mg of protein and primary antibody (DDK, 1:100, OriGene, TA50011-1; tGFP, 1:100, Origene, TA150071) were incubated overnight with rotation at 4 °C. Protein A magnetic beads (Bio-Rad, 1614013) were washed with cold GTIP buffer, and added to lysate samples for another incubation, 4 h at 4 °C. Post incubation, samples were washed with PBS before elution in NuPAGE LDS sample buffer 4X (Invitrogen, NP0008) by heating for 5 min at 95 °C.

Western blotting was performed as previously described[5,14] on a NuPAGE system using 4–12% Bis-Tris SDS-PAGE gels (Invitrogen). The following primary antibodies were used in this study: DDK (Origene, TA100011, 1:1000), ITPR3 (abcam, ab264283, 1:2000), tGFP (Origene, TA150071, 1:1000), and HA (Cell Signaling Technology, C29F4, 1:1000). Donkey anti-rabbit and goat anti-mouse IRDye 680RD and 800CW conjugated secondary antibodies (LI-COR Biosciences, 926-68073 926-68070 926-32213 and 926-32210) were used for infrared imaging with the LICOR Odyssey Infrared Imaging System (LI-COR Biosciences). Image Studio Ver 5.2 was used to prepare images of blots for figures and to quantify band signal with background subtraction. Original uncropped Western blot images included in the manuscript are found in (Supplementary Fig. 1).

Circular dichroism

The experiments with circular dichroism were carried out at the Biophysics Instrumentation Facility (Department of Biochemistry, University of Wisconsin- Madison), as previously described[34]. Human CALR-myc was purified from stably expressing cells using the ProFound c-myc-Tag IP/Co-IP kit (Pierce), as suggested by the manufacturer. The difference in the absorbances of left- and right-handed circularly polarized light impinging on the solution was measured at 25 °C with a 202SF CD Spectrophotometer (Aviv Biomedical) in PBS and at room temperature. Appropriate controls included PBS alone and Ca^{+2} in the absence of CALR. The Biophysics Instrumentation Facility was established by funding from NSF (BIR-9512577), NIH (S10 RR13790) and the University of Wisconsin.

CRISPR

To induce mutations to Ca^{+2}-binding sites in endogenous CALR (D328A and Δ338–408), a homology directed repair (HDR) donor block containing the point mutation and homologous sequences spanning either side of the targeted deletion was designed (see Supplementary Method). Using the 4D-Nucleofector X unit (Lonza, AAF-1003X) with pulse code CM-130, HEK293 cells suspended in SF buffer (Lonza, V4XC-9064) were electroporated with 1.95 µM Cas9V3 (Integrated DNA Technologies, 1081059): 2 µM single guide RNA (Alt-R CRISPR-Cas9 sgRNA, Integrated DNA Technologies, sgRNA targeting sequences: UUCAUCCUCCAGGUCAAGUC & AU GCCUCAUCGUUGGUGAUG) ribonucleoprotein (RNP) complex, 1 µM Alt-R HDR donor block (Integrated DNA Technologies), and 1 µM electroporation enhancer (Integrated DNA Technologies, 1075916). Five days post electroporation, the University of Wisconsin Flow Cytometry Core Facility performed Fluorescence Assisted Cell Sorting (FACS) on transfected cells stained with Ghost Dye Red 780 (Cytek, 13-0865-T100) to plate single, live cells in 96 well plates. PCR screening of amplified colonies using PrimeSTAR GXL DNA Polymerase (Takara, R050A) was initially used to indirectly detect the targeted deletion. The following primers were used: forward- G TGTTAGCCAGGGTGGTCTC and reverse- AGGGCTGAAGGAGAATCAAAG. Digital PCR (dPCR) analysis for copy number variation (CNV) with the QuantStudio Absolute Q dPCR system (Thermo Fisher Scientific) revealed two copies of the mutated locus. The following primers and probes were used for the target allele (mutated CALR, forward- CAGGTCAAGAGCGGAACTATT, reverse- CTACAGCTCGTCCTTGGC, probe-CAAATGACGAAGCTGTGCCTGGC) and reference allele (RNaseP, forward- AGATTTGGACCTGCGAGC G, reverse- GAGCGGCTGTCTCCACAAGT, probe- TTCTGACCTGAAGGCTCTGCGCG). Amplicons were sequenced at the University of Wisconsin DNA sequencing facility. No clones were homozygous for the exact D328A + Δ338–408 intended allele. The clone used for experimentation ($CALR^{CR}$) was heterozygous for the exact D328A + Δ338–408 intended edit while the other allele carried a K322N + Δ323–411 edit. This maintained in-frame sequence coding sequence and targeted both Ca^{+2}-binding sites.

Immunocytochemistry

HEK293 cells plated on poly-D-lysine coated glass coverslips co-transfected ERmCherry and ATG9A-tGFP were fixed in 4% paraformaldehyde for 10 min (Thermo Fisher Scientific, J19943-K2) and permeabilized with 0.1% Triton TM-X100 (Roche Applied Biosciences, 11332481001) for 5 min followed by a 1 h incubation in blocking buffer (10% BSA, 5% goat serum in PBS). To increase signal, cells were stained with mCherry (Novus Biologicals, NBP196752, 1:1000) and tGFP (Origene, TA150071, 1:500) primary antibodies. Primary cultured MEFs (WT, AT-$1^{S113R/+}$, AT-1 sTg) were plated on uncoated glass coverslips and co-transfected with ATG9A-mCherry and SEC13-tGFP. 24 h post transfection, cells were fixed in paraformaldehyde for 10 min (Thermo Fisher Scientific, J19943-K2), washed in PBS and coverslips were mounted on slides with Fluoro-Gel II with DAPI (Electron Microscopy Sciences, 17985-50). Primary MEFs (WT, AT-$1^{S113R/+}$, AT-1 sTg) were plated on glass bottomed plates and transfected with ATG9A-EATR. 4 h prior to imaging, the media was changed to fresh DMEM or EBSS to simulate fed and starved conditions respectively. All fluorescently labeled cells were imaged on a Nikon A1 inverted confocal microscope using NIS-Elements AR version v 5.2 software with 405 nm (blue channel), 488 (green channel), 561 nm (red channel), and 640 nm (far red channel) laser wavelengths using the Galvano scan head. Z-stack 1024 × 1024 images were acquired using a 60x or 100x oil objective (NA = 1.4). IMARIS v 10.0.0 was used for subsequent image analysis for volume rendering and co-localization analysis. For the MEF experiments, n refers to the number of cells with 3 biologically independent cell lines used for each genotype.

Statistics

Data analysis was performed in Graphpad Prism v 9.3.1. Data are presented as mean ± standard deviation unless otherwise stated. Statistical outliers were detected using the ROUT method (Q = 10%). Comparison of means was performed using Student's t-test for two groups or one-way ANOVA for three or more groups followed by a Dunnett's multiple comparison test (comparison to one control group) for compound treatments or followed by a Tukey's multiple comparisons test (comparison among all groups) for AT-1 experiments. Differences were declared statistically significant if $p < 0.05$, and the following statistical significance indicators are used: $^{*}p < 0.05$, $^{**}p < 0.01$, $^{***}p < 0.001$, $\#p < 0.0001$.

Data availability

The authors declare that all other data supporting the findings of this study are available within the paper and its supplementary material.

Received: 22 August 2024; Accepted: 17 October 2024
Published online: 26 October 2024

References

1. Fernandez-Fuente, G., Rigby, M. J. & Puglielli, L. Intracellular citrate/acetyl-CoA flux and endoplasmic reticulum acetylation: Connectivity is the answer. *Mol. Metab.***67**, 101653. https://doi.org/10.1016/j.molmet.2022.101653 (2023).
2. Nieborak, A. & Schneider, R. Metabolic intermediates - cellular messengers talking to chromatin modifiers. *Mol. Metab.***14**, 39–52. https://doi.org/10.1016/j.molmet.2018.01.007 (2018).
3. Kaelin, W. G. Jr & McKnight, S. L. Influence of metabolism on epigenetics and disease. *Cell***153**, 56–69. https://doi.org/10.1016/j.cell.2013.03.004 (2013).
4. Pehar, M., Jonas, M. C., Hare, T. M. & Puglielli, L. SLC33A1/AT-1 protein regulates the induction of autophagy downstream of IRE1/XBP1 pathway. *J. Biol. Chem.***287**, 29921–29930. https://doi.org/10.1074/jbc.M112.363911 (2012).
5. Peng, Y. et al. Deficient import of Acetyl-CoA into the ER lumen causes neurodegeneration and propensity to infections, inflammation, and Cancer. *J. Neurosci.***34**, 6772–6789. https://doi.org/10.1523/JNEUROSCI.0077-14.2014 (2014).
6. Peng, Y. et al. Increased transport of acetyl-CoA into the endoplasmic reticulum causes a progeria-like phenotype. *Aging Cell.* e12820. https://doi.org/10.1111/acel.12820 (2018).
7. Rigby, M. J. et al. Endoplasmic reticulum acetyltransferases Atase1 and Atase2 differentially regulate reticulophagy, macroautophagy and cellular acetyl-CoA metabolism. *Commun. Biol.***4**, 454. https://doi.org/10.1038/s42003-021-01992-8 (2021).
8. Fernandez-Fuente, G. et al. The citrate transporters SLC13A5 and SLC25A1 elicit different metabolic responses and phenotypes in the mouse. *Commun. Biol.***6**, 926. https://doi.org/10.1038/s42003-023-05311-1 (2023).
9. Peng, Y. et al. Improved proteostasis in the secretory pathway rescues Alzheimer's disease in the mouse. *Brain*. **139**, 937–952. https://doi.org/10.1093/brain/awv385 (2016).
10. Murie, M. et al. ATase inhibition rescues age-associated proteotoxicity of the secretory pathway. *Commun. Biol.***5**, 173. https://doi.org/10.1038/s42003-022-03118-0 (2022).
11. Hullinger, R. et al. Increased expression of AT-1/SLC33A1 causes an autistic-like phenotype in mice by affecting dendritic branching and spine formation. *J. Exp. Med.***213**, 1267–1284. https://doi.org/10.1084/jem.20151776 (2016).
12. Rigby, M. J. et al. Increased expression of SLC25A1/CIC causes an autistic-like phenotype with altered neuron morphology. *Brain*https://doi.org/10.1093/brain/awab295 (2022).
13. Rigby, M. J. et al. SLC13A5/sodium-citrate co-transporter overexpression causes disrupted white matter integrity and an autistic-like phenotype. *Brain Commun.***4**, fcac002. https://doi.org/10.1093/braincomms/fcac002 (2022).
14. Sheehan, B. K., Orefice, N. S., Peng, Y., Shapiro, S. L. & Puglielli, L. ATG9A regulates proteostasis through reticulophagy receptors FAM134B and SEC62 and folding chaperones CALR and HSPB1. *iScience***24**, 102315. https://doi.org/10.1016/j.isci.2021.102315 (2021).
15. Liang, J. R., Lingeman, E., Ahmed, S. & Corn, J. E. Atlastins remodel the endoplasmic reticulum for selective autophagy. *J. Cell. Biol.***217**, 3354–3367. https://doi.org/10.1083/jcb.201804185 (2018).
16. Daverkausen-Fischer, L. & Prols, F. Regulation of calcium homeostasis and flux between the endoplasmic reticulum and the cytosol. *J. Biol. Chem.***298**, 102061. https://doi.org/10.1016/j.jbc.2022.102061 (2022).
17. Engedal, N. et al. Modulation of intracellular calcium homeostasis blocks autophagosome formation. *Autophagy***9**, 1475–1490. https://doi.org/10.4161/auto.25900 (2013).
18. Villamil Giraldo, A. M. et al. The structure of calreticulin C-terminal domain is modulated by physiological variations of calcium concentration. *J. Biol. Chem.***285**, 4544–4553. https://doi.org/10.1074/jbc.M109.034512 (2010).

19. Young, A. R. et al. Starvation and ULK1-dependent cycling of mammalian Atg9 between the TGN and endosomes. *J. Cell. Sci.***119**, 3888–3900 (2006).
20. Tamura, H., Shibata, M., Koike, M., Sasaki, M. & Uchiyama, Y. Atg9A protein, an autophagy-related membrane protein, is localized in the neurons of mouse brains. *J. Histochem. Cytochem.***58**, 443–453 (2010).
21. Ohashi, Y. & Munro, S. Membrane delivery to the yeast autophagosome from the golgi-endosomal system. *Mol. Biol. Cell.***21**, 3998–4008 (2010).
22. Puri, C., Renna, M., Bento, C. F., Moreau, K. & Rubinsztein, D. C. Diverse autophagosome membrane sources coalesce in recycling endosomes. *Cell***154**, 1285–1299. https://doi.org/10.1016/j.cell.2013.08.044 (2013).
23. Bejarano, E. et al. Connexins modulate autophagosome biogenesis. *Nat. Cell. Biol.***16**, 401–414. https://doi.org/10.1038/ncb2934 (2014).
24. Saitoh, T. et al. Atg9a controls dsDNA-driven dynamic translocation of STING and the innate immune response. *Proc. Natl. Acad. Sci. USA***106**, 20842–20846. https://doi.org/10.1073/pnas.0911267106 (2009).
25. Sawa-Makarska, J. et al. Reconstitution of autophagosome nucleation defines Atg9 vesicles as seeds for membrane formation. *Science***369**https://doi.org/10.1126/science.aaz7714 (2020).
26. Claude-Taupin, A. et al. ATG9A protects the plasma membrane from programmed and incidental permeabilization. *Nat. Cell. Biol.***23**, 846–858. https://doi.org/10.1038/s41556-021-00706-w (2021).
27. van Vliet, A. R. et al. Exploring the ATG9A interactome uncovers interaction with VPS13A. *J. Cell. Sci.***137**https://doi.org/10.1242/jcs.261081 (2024).
28. Carreras-Sureda, A., Pihan, P. & Hetz, C. Calcium signaling at the endoplasmic reticulum: Fine-tuning stress responses. *Cell. Calcium***70**, 24–31. https://doi.org/10.1016/j.ceca.2017.08.004 (2018).
29. Guardia, C. M. et al. Structure of human ATG9A, the only transmembrane protein of the core autophagy machinery. *Cell. Rep.***31**, 107837. https://doi.org/10.1016/j.celrep.2020.107837 (2020).
30. Lai, L. T. F. et al. Subnanometer resolution cryo-EM structure of Arabidopsis thaliana ATG9. *Autophagy***16**, 575–583. https://doi.org/10.1080/15548627.2019.1639300 (2020).
31. Maeda, S. et al. Structure, lipid scrambling activity and role in autophagosome formation of ATG9A. *Nat. Struct. Mol. Biol.***27**https://doi.org/10.1038/s41594-020-00520-2 (2020).
32. Matoba, K. et al. Atg9 is a lipid scramblase that mediates autophagosomal membrane expansion. *Nat. Struct. Mol. Biol.***27**https://doi.org/10.1038/s41594-020-00518-w (2020).
33. Dieterich, I. A. et al. Acetyl-CoA flux from the cytosol to the ER regulates engagement and quality of the secretory pathway. *Sci. Rep.***11**, 2013. https://doi.org/10.1038/s41598-021-81447-6 (2021).
34. Ding, Y. et al. Biochemical inhibition of the acetyltansferases ATase1 and ATase2 reduces b-secretase (BACE1) levels and ab generation. *J. Biol. Chem.***287**, 8424–8433 (2012).

Acknowledgements

The Puglielli laboratory is funded by the NINDS (R01 NS094154), NIGMS (R01 GM148487), and the NIA (R01 AG078794). This research was also supported by a core grant to the Waisman Center from NICHD-U54 HD105353. The Biotechnology Center's Advanced Genome Editing Laboratory (RRID: SCR_021070) and the Flow Cytometry Laboratory were supported by the University of Wisconsin Carbone Cancer Center through the National Cancer Institute (P30 CA014520). We would like to thank the members of the Puglielli lab for their critical suggestions.

Author contributions

M.M.B., B.K.S., S.L.S., Y.D., C.D.R., and B.P.L. performed the experiments and analyzed the data. L.P. designed the overall study and provided advice for the experiments. M.M.B. and L.P. wrote the manuscript with input from all authors.

Declarations

Competing interests

The authors declare the following competing interests: L.P. is a consultant for Belharra Therapeutics. The remaining authors have no competing interests to disclose.

Additional information

Supplementary Information The online version contains supplementary material available at https://doi.org/10.1038/s41598-024-76854-4.

Correspondence and requests for materials should be addressed to L.P.